# Electronic supplementary information (ESI)

## Coordination networks constructed from a flexible ligand: single-crystal-to-single-crystal transformations, thermoresponsive and electrochemical performances

Jinjiao Zhu[†], Yajun Sun[†], Weilinsen Ding[†], Peiyuan Li, Qingyang Pang, Xinwen Dou, Li Bian, Qiang Ju and Zhenlan Fang*

Key Laboratory of Flexible Electronics (KLOFE) & Institute of Advanced Materials (IAM), Jiangsu National Synergetic Innovation Center for Advanced Materials (SICAM), Nanjing Tech University (NanjingTech), 30 South Puzhu Road, Nanjing 211816, P.R. China.
Email: iamzlfang@njtech.edu.cn

# Table of Contents

# Crystal Data

**Table S1.** Crystal data and structure refinement results for **1a**, **1b**, **1c** and **1d**.

| 2-D CNs | **1a** | **1b** | **1c** | **1d** |
|---|---|---|---|---|
| Temp (K) | 298(2) | 100(2) | 298(2) | 100(2) |
| Color | Yellow | Yellow | Green | Green |
| Empirical formula | $Cu_2Cl_2C_{16}N_4O_2H_{18}$ | $Cu_2Cl_2C_{16}N_4O_2H_{18}$ | $Cu_2Cl_2C_{16}N_4O_2H_{18}$ | $Cu_2Cl_2C_{16}N_4O_2H_{18}$ |
| Formula weight | 496.32 | 496.32 | 496.32 | 496.32 |
| Crystal system | Monoclinic | Monoclinic | Monoclinic | Monoclinic |
| Space group | *P*2/*c* | *P*2/*c* | *P*2/*c* | *P*2/*c* |
| *Z* | 4 | 4 | 4 | 4 |
| *a* (Å) | 12.892(17) | 12.392(1) | 12.543(2) | 12.379(1) |
| *b* (Å) | 9.895(13) | 9.495(1) | 9.541(1) | 9.493(1) |
| *c* (Å) | 17.430(20) | 16.906(1) | 16.985(2) | 16.918(2) |
| $\alpha$ (deg) | 90 | 90 | 90 | 90 |
| $\beta$ (deg) | 105.86(3) | 106.07(0) | 106.37(0) | 106.04(0) |
| $\gamma$ (deg) | 90 | 90 | 90 | 90 |
| *V* (Å$^3$) | 2139.0(5) | 1911.5(2) | 1950.4(4) | 1910.8(4) |
| $\rho_{calcd}$ (g/cm$^3$) | 1.541 | 1.725 | 1.690 | 1.725 |
| $\mu$ (mm$^{-1}$) | 2.254 | 2.523 | 2.472 | 2.524 |
| GOF | 1.000 | 1.063 | 1.049 | 1.022 |
| $R_1$ (I>2σ(I))[a] | 0.0429 | 0.0329 | 0.0451 | 0.0343 |
| $wR_2$ (I>2σ(I))[a] | 0.1119 | 0.0868 | 0.1201 | 0.0914 |
| $R_1$ (all data)[b] | 0.0863 | 0.0451 | 0.0924 | 0.0507 |
| $wR_2$ (all data)[b] | 0.1393 | 0.1017 | 0.1538 | 0.1080 |

[a] $R_1 = \sum||F_o| - |F_c||/\sum|F_o|$; [b] $wR_2 = \sum\{w(F_o^2 - F_c^2)^2/\sum[w(F_o^2)^2]\}^{1/2}$

**Table S2.** Crystal data and structure refinement results for **2a**,[1] **2b**,[1] **2c** and **2d**.

| 2-D CNs | **2a**[1] | **2b**[1] | **2c** | **2d** |
|---|---|---|---|---|
| Temp (K) | 298(2) | 100(2) | 298(2) | 100(2) |
| Color | Yellow | Yellow | Green | Green |
| Empirical formula | $Cu_2Br_2C_{16}N_4O_2H_{18}$ | $Cu_2Br_2C_{16}N_4O_2H_{18}$ | $Cu_2Br_2C_{16}N_4O_2H_{18}$ | $Cu_2Br_2C_{16}N_4O_2H_{18}$ |
| Formula weight | 585.24 | 585.24 | 585.24 | 585.24 |
| Crystal system | Monoclinic | Monoclinic | Monoclinic | Monoclinic |
| Space group | *P*2/*c* | *P*2/*c* | *P*2/*c* | *P*2/*c* |
| *Z* | 4 | 4 | 4 | 4 |
| *a* (Å) | 13.052(2) | 12.954(2) | 13.097(2) | 13.012(1) |
| *b* (Å) | 9.646(1) | 9.607(2) | 9.681(2) | 9.653(1) |
| *c* (Å) | 16.719(3) | 16.614(3) | 16.800(3) | 16.709(2) |
| $\alpha$ (deg) | 90 | 90 | 90 | 90 |
| $\beta$ (deg) | 107.56(1) | 107.51(1) | 107.54(1) | 107.45(0) |
| $\gamma$ (deg) | 90 | 90 | 90 | 90 |
| *V* (Å$^3$) | 2006.8(6) | 1971.8(6) | 2031.1(6) | 2002.1(3) |
| $\rho_{calcd}$ (g/cm$^3$) | 1.937 | 1.971 | 1.914 | 1.942 |
| $\mu$ (mm$^{-1}$) | 6.119 | 6.227 | 6.046 | 6.133 |
| GOF | 1.040 | 1.026 | 1.015 | 1.005 |
| $R_1$ (I>2σ(I))[a] | 0.0422 | 0.0414 | 0.0390 | 0.0496 |
| $wR_2$ (I>2σ(I))[a] | 0.0926 | 0.1048 | 0.0817 | 0.1059 |
| $R_1$ (all data)[b] | 0.1201 | 0.0737 | 0.0745 | 0.0880 |
| $wR_2$ (all data)[b] | 0.1285 | 0.1268 | 0.0959 | 0.1224 |

[a] $R_1 = \sum||F_o| - |F_c||/\sum|F_o|$; [b] $wR_2 = \sum\{w(F_o^2 - F_c^2)^2/\sum[w(F_o^2)^2]\}^{1/2}$

**Table S3.** Selected bond lengths (Å) and angles (°) for **1a**-**1d**.

| **1a** | | **1b** | | **1c** | | **1d** | |
|---|---|---|---|---|---|---|---|
| Cu(2)-N(1) | 2.103(4) | Cu(2)-N(1) | 2.034(3) | Cu(2)-N(1) | 2.039(4) | Cu(2)-N(1) | 2.033(2) |
| Cu(2)-Cl(1) | 2.266(2) | Cu(2)-Cl(1) | 2.2143(10) | Cu(2)-Cl(1) | 2.2130(14) | Cu(2)-Cl(1) | 2.2153(8) |
| Cu(2)-Cl(2) | 2.332(3) | Cu(2)-Cl(2) | 2.2573(10) | Cu(2)-Cl(2) | 2.2557(14) | Cu(2)-Cl(2) | 2.2553(8) |
| Cu(1)-N(4)#2 | 2.076(4) | Cu(1)-N(4)#1 | 2.009(3) | Cu(1)-N(4)#1 | 2.013(3) | Cu(1)-N(4)#1 | 2.015(2) |
| Cu(1)-Cl(1) | 2.303(3) | Cu(1)-Cl(1) | 2.2279(10) | Cu(1)-Cl(1) | 2.2220(13) | Cu(1)-Cl(1) | 2.2311(8) |
| Cu(1)-Cl(2)#1 | 2.344(3) | Cu(1)-Cl(2)#2 | 2.2668(10) | Cu(1)-Cl(2)#2 | 2.2687(13) | Cu(1)-Cl(2)#2 | 2.2707(8) |
| Cu(2)-Cu(1)#1 | 2.801(3) | Cu(2)-Cu(1)#2 | 2.6680(6) | Cu(2)-Cu(1)#2 | 2.7112(8) | Cu(2)-Cu(1)#2 | 2.6627(5) |
| Cu(1)-Cu(2) | 2.849(3) | Cu(1)-Cu(2) | 2.6991(6) | Cu(1)-Cu(2) | 2.7647(8) | Cu(1)-Cu(2) | 2.6983(5) |
| Cu(1)-Cu(2)#1 | 2.801(3) | Cu(1)-Cu(2)#2 | 2.6680(6) | Cu(1)-Cu(2)#2 | 2.7112(8) | Cu(1)-Cu(2)#2 | 2.6627(5) |
| - | - | Cu(1)-Cu(1)#2 | 3.0171(9) | Cu(1)-Cu(1)#2 | 3.0560(13) | Cu(1)-Cu(1)#2 | 3.0118(8) |
| N(1)-Cu(2)-Cl(1) | 114.71(11) | N(1)-Cu(2)-Cl(1) | 113.81(9) | N(1)-Cu(2)-Cl(1) | 115.25(10) | N(1)-Cu(2)-Cl(1) | 113.61(7) |
| N(1)-Cu(2)-Cl(2) | 110.23(13) | N(1)-Cu(2)-Cl(2) | 108.91(9) | N(1)-Cu(2)-Cl(2) | 109.45(11) | N(1)-Cu(2)-Cl(2) | 108.99(7) |
| Cl(1)-Cu(2)-Cl(2) | 131.74(6) | Cl(1)-Cu(2)-Cl(2) | 134.24(4) | Cl(1)-Cu(2)-Cl(2) | 132.03(6) | Cl(1)-Cu(2)-Cl(2) | 134.39(3) |
| N(4)#2-Cu(1)-Cl(1) | 119.51(13) | N(4)#1-Cu(1)-Cl(1) | 118.67(9) | N(4)#1-Cu(1)-Cl(1) | 119.34(11) | N(4)#1-Cu(1)-Cl(1) | 118.49(7) |
| N(4)#2-Cu(1)-Cl(2)#1 | 107.28(11) | N(4)#1-Cu(1)-Cl(2)#2 | 106.04(9) | N(4)#1-Cu(1)-Cl(2)#2 | 107.43(10) | N(4)#1-Cu(1)-Cl(2)#2 | 106.04(7) |
| Cl(1)-Cu(1)-Cl(2)#1 | 129.30(7) | Cl(1)-Cu(1)-Cl(2)#2 | 130.78(4) | Cl(1)-Cu(1)-Cl(2)#2 | 129.23(6) | Cl(1)-Cu(1)-Cl(2)#2 | 130.97(3) |

Symmetry transformations used to generate equivalent atoms: **1a**: (#1) -x, y, -z+1/2; (#2) -x+1, y-1, -z+1/2; **1b**: (#1) -x-1, y-1, -z+1/2; (#2) -x-2, y, -z+1/2; **1c**: (#1) -x-1, y-1, -z+3/2; (#2) -x-2, y, -z+3/2; **1d**: (#1) -x-1, y-1, -z+1/2; (#2) -x, y, -z+1/2.

**Table S4.** Selected bond lengths (Å) and angles (°) for **2a**-**2d**.

| **2a**[1] | | **2b**[1] | | **2c** | | **2d** | |
|---|---|---|---|---|---|---|---|
| Cu(2)-N(1) | 2.022(4) | Cu(2)-N(1) | 2.021(4) | Cu(2)-N(1) | 2.029(4) | Cu(2)-N(1) | 2.031(4) |
| Cu(2)-Br(1) | 2.3385(10) | Cu(2)-Br(1) | 2.3376(9) | Cu(2)-Br(1) | 2.3489(10) | Cu(2)-Br(1) | 2.3504(9) |
| Cu(2)-Br(2) | 2.3992(10) | Cu(2)-Br(2) | 2.3939(8) | Cu(2)-Br(2) | 2.4068(10) | Cu(2)-Br(2) | 2.4034(8) |
| Cu(1)-N(4)#2 | 1.998(4) | Cu(1)-N(4)#2 | 1.992(4) | Cu(1)-N(4)#2 | 2.004(4) | Cu(1)-N(4)#1 | 2.006(4) |
| Cu(1)-Br(1) | 2.3538(10) | Cu(1)-Br(1) | 2.3576(8) | Cu(1)-Br(1) | 2.3636(9) | Cu(1)-Br(1) | 2.3677(8) |
| Cu(1)-Br(2)#2 | 2.4002(10) | Cu(1)-Br(2)#2 | 2.3993(8) | Cu(1)-Br(2)#1 | 2.4086(10) | Cu(1)-Br(2)#2 | 2.4121(8) |
| Cu(2)-Cu(1)#2 | 2.6241(10) | Cu(2)-Cu(1)#2 | 2.5815(9) | Cu(2)-Cu(1)#1 | 2.6356(10) | Cu(2)-Cu(1)#2 | 2.5971(9) |
| Cu(1)-Cu(2) | 2.7756(11) | Cu(1)-Cu(2) | 2.7064(9) | Cu(1)-Cu(2) | 2.7878(10) | Cu(1)-Cu(2) | 2.7213(9) |
| Cu(1)-Cu(2)#2 | 2.6241(10) | Cu(1)-Cu(2)#2 | 2.5815(9) | Cu(1)-Cu(2)#1 | 2.6356(10) | Cu(1)-Cu(2)#2 | 2.5971(9) |
| Cu(1)-Cu(1)#2 | 2.9126(18) | Cu(1)-Cu(1)#2 | 2.8769(14) | Cu(1)-Cu(1)#1 | 2.9266(17) | Cu(1)-Cu(1)#2 | 2.8969(15) |
| - | - | Cu(2)-Cu(2)#2 | 3.0564(14) | - | - | - | - |
| N(1)-Cu(2)-Br(1) | 113.10(13) | N(1)-Cu(2)-Br(1) | 112.02(12) | N(1)-Cu(2)-Br(1) | 113.21(13) | N(1)-Cu(2)-Br(1) | 112.05(12) |
| N(1)-Cu(2)-Br(2) | 109.21(13) | N(1)-Cu(2)-Br(2) | 108.42(12) | N(1)-Cu(2)-Br(2) | 109.11(13) | N(1)-Cu(2)-Br(2) | 108.52(12) |
| Br(1)-Cu(2)-Br(2) | 127.49(4) | Br(1)-Cu(2)-Br(2) | 129.75(3) | Br(1)-Cu(2)-Br(2) | 127.42(4) | Br(1)-Cu(2)-Br(2) | 129.66(4) |
| N(4)#1-Cu(1)-Br(1) | 120.96(13) | N(4)#1-Cu(1)-Br(1) | 119.95(12) | N(4)#2-Cu(1)-Br(1) | 120.86(13) | N(4)#1-Cu(1)-Br(1) | 119.94(13) |
| N(4)#1-Cu(1)-Br(2)#2 | 107.05(12) | N(4)#1-Cu(1)-Br(2)#2 | 106.00(11) | N(4)#2-Cu(1)-Br(2)#1 | 107.21(12) | N(4)#1-Cu(1)-Br(2)#2 | 106.13(12) |
| Br(1)-Cu(1)-Br(2)#2 | 124.55(4) | Br(1)-Cu(1)-Br(2)#2 | 125.82(3) | Br(1)-Cu(1)-Br(2)# | 124.58(4) | Br(1)-Cu(1)-Br(2)#2 | 125.80(3) |

Symmetry transformations used to generate equivalent atoms: **2a-b:** (#1) -x, y-1, -z+3/2; (#2) -x-1, y, -z+3/2; **2c**: (#1) -x+3, y, -z+1/2; (#2) -x+2, y-1, -z+1/2; **2d**: (#1) -x+3, y-1, -z+1/2; (#2) -x+4, y, -z+1/2.

**Table S5.** Table of the hydrogen bonds for **1a**-**1d** and **2a**-**2d**.

| | | | | |
|---|---|---|---|---|
| **1a** | the inter hydrogen bonds in 2-D interpenetrating layer | Cl2⋯H15 = 3.018 Å | Cl2⋯C15 = 3.633 Å | ∠Cl2⋯H15⋯C15 = 125.033º |
| | the hydrogen bonds between 2-D interpenetrating layers | Cl2⋯H9A = 2.903 Å | Cl2⋯C9 = 3.809 Å | ∠Cl2⋯H3A⋯C9 = 155.913º |
| **1b** | the inter hydrogen bonds in 2-D interpenetrating layer | Cl2⋯H15 = 2.830 Å | Cl2⋯C15 =3.465 Å | ∠Cl2⋯H15⋯C15 = 125.130º |
| | the hydrogen bonds between 2-D interpenetrating layers | Cl2⋯H9A = 2.722 Å | Cl2⋯C9 = 3.639 Å | ∠Cl2⋯H9A⋯C9 = 154.203º |
| | the hydrogen bonds between 2-D interpenetrating layers | Cl1⋯H13 = 2.975 Å | Cl1⋯C13 = 3.477 Å | ∠Cl1⋯H13⋯C13 = 114.388º |
| **1c** | the inter hydrogen bonds in 2-D interpenetrating layer | Cl2⋯H15 = 2.898 Å | Cl2⋯C15 = 3.516 Å | ∠Cl2⋯H15⋯C15 = 125.034º |
| | the hydrogen bonds between 2-D interpenetrating layers | Cl2⋯H9A = 2.781 Å | Cl2⋯C9 = 3.685 Å | ∠Cl2⋯H9A⋯C9 = 155.482º |
| **1d** | the inter hydrogen bonds in 2-D interpenetrating layer | Cl2⋯H15 =2.821 Å | Cl2⋯C15 = 3.458 Å | ∠Cl2⋯H15⋯C15 = 125.328º |
| | the hydrogen bonds between 2-D interpenetrating layers | Cl2⋯H9A = 2.720 Å | Cl2⋯C9 = 3.634 Å | ∠Cl2⋯H9A⋯C9 = 153.703º |
| **2a**[1] | the inter hydrogen bonds in 2-D interpenetrating layer | Br2⋯H15 = 2.915 Å | Br2⋯C15 = 3.559 Å | ∠Br2⋯H15⋯C15 = 127.539º |
| | the hydrogen bonds between 2-D interpenetrating layers | Br2⋯H9A = 2.899 Å | Br2⋯C9 = 3.786 Å | ∠Br2⋯H8A⋯C9 = 152.521º |
| **2b**[1] | the inter hydrogen bonds in 2-D interpenetrating layer | Br2⋯H15 = 2.865 Å | Br2⋯C15 = 3.521 Å | ∠Br2⋯H15⋯C15 = 127.208º |
| | the hydrogen bonds between 2-D interpenetrating layers | Br2⋯H9A = 2.853 Å | Br2⋯C9 = 3.743 Å | ∠Br2⋯H7A⋯C9 = 150.037º |
| **2c** | the inter hydrogen bonds in 2-D | Br2⋯H15 = 2.929 Å | Br2⋯C15 = 3.577 Å | ∠Br2⋯H15⋯C15 = 127.952º |

| | | | | |
|---|---|---|---|---|
| | interpenetrating layer | | | |
| | the hydrogen bonds between 2-D interpenetrating layers | Br2⋯H9A = 2.909 Å | Br2⋯C9 = 3.801 Å | ∠Br2⋯H9A⋯C9 = 153.320º |
| **2d** | the inter hydrogen bonds in 2-D interpenetrating layer | Br2⋯H15 = 2.881 Å | Br2⋯C15 = 3.545 Å | ∠Br2⋯H15⋯C15 = 127.947º |
| | the hydrogen bonds between 2-D interpenetrating layers | Br2⋯H9A = 2.877 Å | Br2⋯C9 = 3.770 Å | ∠Br2⋯H9A⋯C9 = 150.382º |

# Structure of Ligands

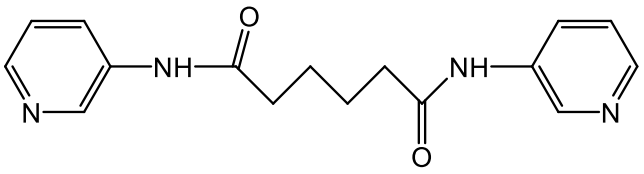


(L1)

*N*,*N*'-bis(3-pyridyl)adipoamide

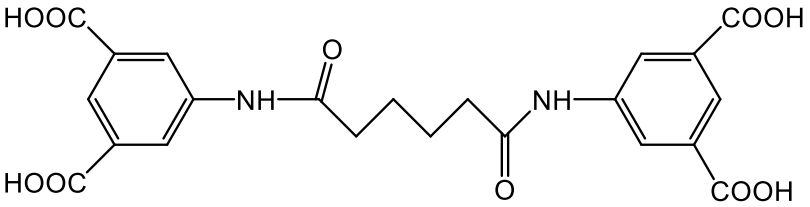


(L2)

5,5'-(adipoylbis(azanediyl))diisophthalic acid

**Scheme 1.** The structure of ligands L1 and L2.

## Powder X-ray Patterns

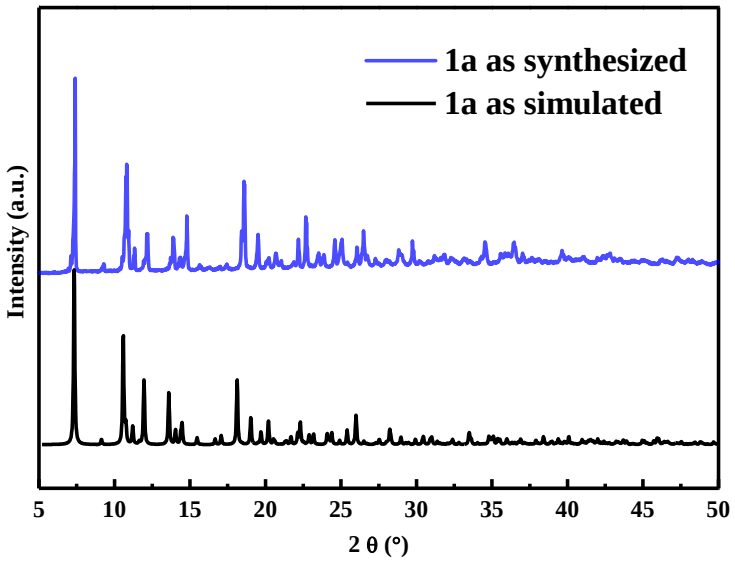


**Figure S1.** Simulated and experimental powder X-ray patterns for **1a**.

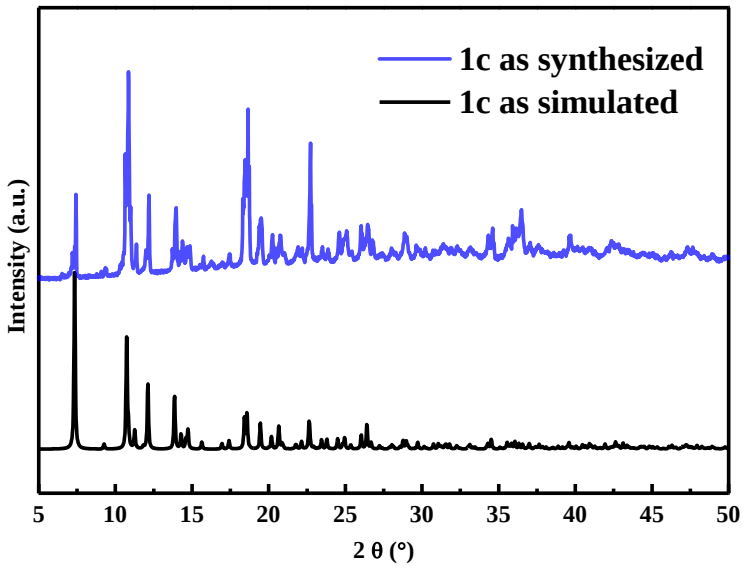


**Figure S2.** Simulated and experimental powder X-ray patterns for **1c**.

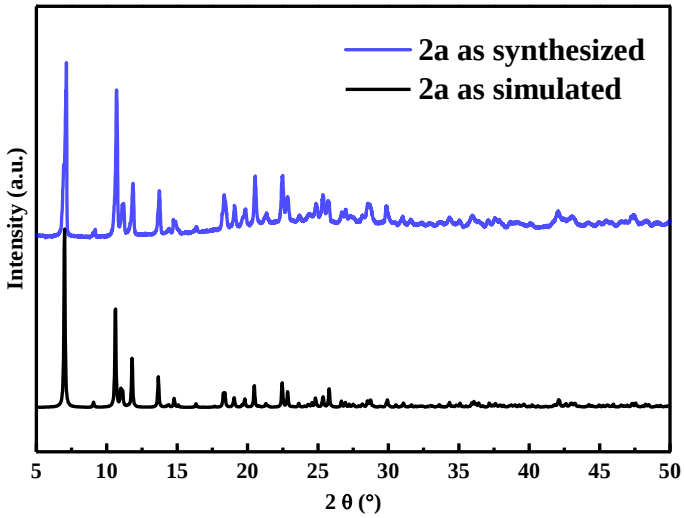


**Figure S3.** Simulated and experimental powder X-ray patterns for **2a**.

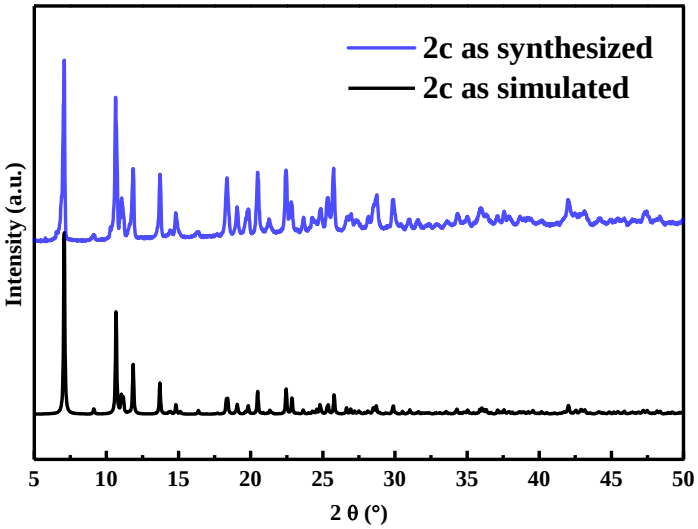


**Figure S4.** Simulated and experimental powder X-ray patterns for **2c**.

The phase purity of all bulk materials has been demonstrated by that the experimental powder X-ray diffraction (PXRD) patterns of **1a**, **1c**, **2a**, **2c** match quite well with the simulated patterns obtained from the single-crystal X-ray data (Figure S1-S4).

# FT-IR Spectra

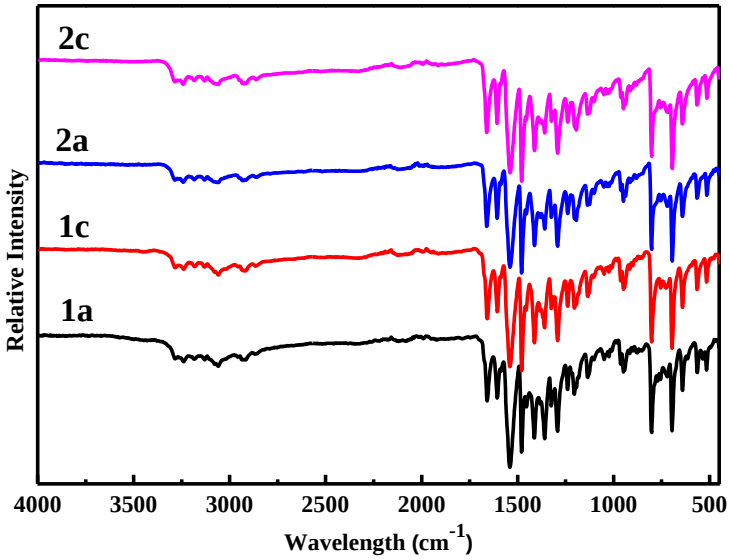


**Figure S5.** FT-IR spectra of **1a**, **1c**, **2a** and **2c.**

The bands centered at ~1415, ~1538 and ~1662 $cm^{-1}$ can be assigned to the stretching vibrations of the pyridine groups, the imine groups (N-H) and the carbonyl groups (C=O) of ligand *N*,*N*'-bis(3-pyridyl)adipoamide. The bands centered at ~3062, ~1603, ~1479 $cm^{-1}$ can be ascribed to the vibrations of C-H, C-C, C-N bonds, respectively. The high similarity between these four samples demonstrates they belong to same structure.

## Thermal Gravimetric Analysis

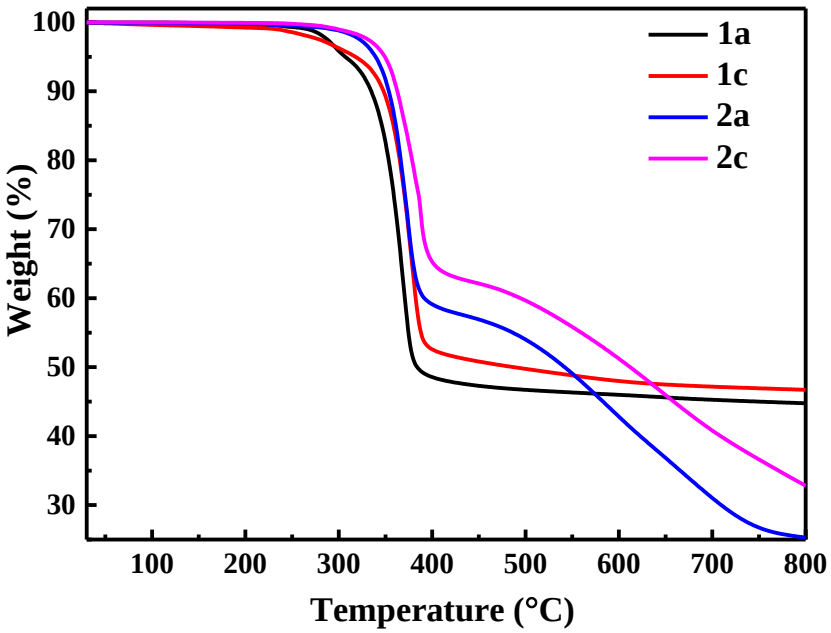


**Figure S6.** The TGA curves of **1a**, **1c**, **2a** and **2c**.

TGA curves of them show that the bromide-based CNs **2a** and **2c** exhibit higher thermal stability than that of the chloride-based CNs **1a** and **1c**, and the green $Cu^{2+}$ samples are more stable than the yellow $Cu^{1+}$ samples. These results demonstrate that the halogen atoms and electronic-structure of copper atoms play a critical role in the thermal stability of these CNs.

## Electrochemical Data

Cyclic voltammetry (CV) tests were performed at different scan rates (1, 2, 5, 10, 20, 50 mV $s^{-1}$) in a potential window of 0-0.5 V. The specific capacitance (*C*) calculated according to the CV curves of **1a**, **1c**, **2a**, **2c** electrode material can be obtained using the equations below[2]:

$$C = \frac{\int idV}{\nu \Delta V m}$$

where $i$ is the current (A), $V$ is the potential (V), $\Delta V$ is the whole voltage scan window, $\nu$ is the scan rate (mV $s^{-1}$), and $m$ is the mass of active materials (g).

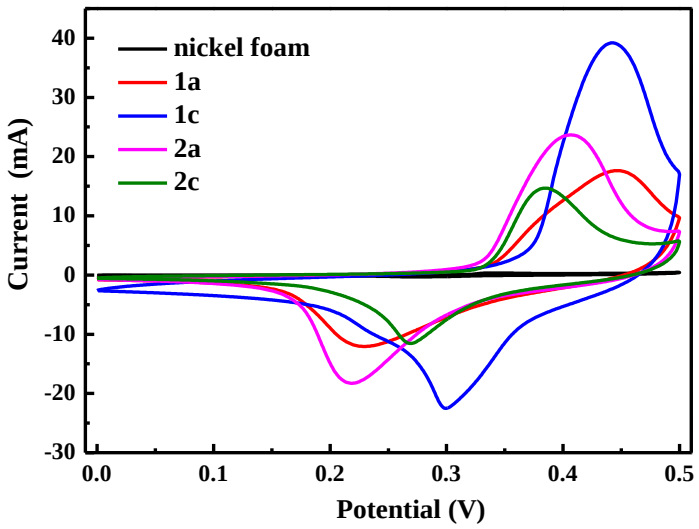


**Figure S7.** The CV curves of nickel foam, **1a**, **1c**, **2a** and **2c**.

The comparison of the CV curves shows that the contribution of nickel foam to the capacitance of these tested samples **1a**, **1c**, **2a** and **2c** is very low and can be ignored.

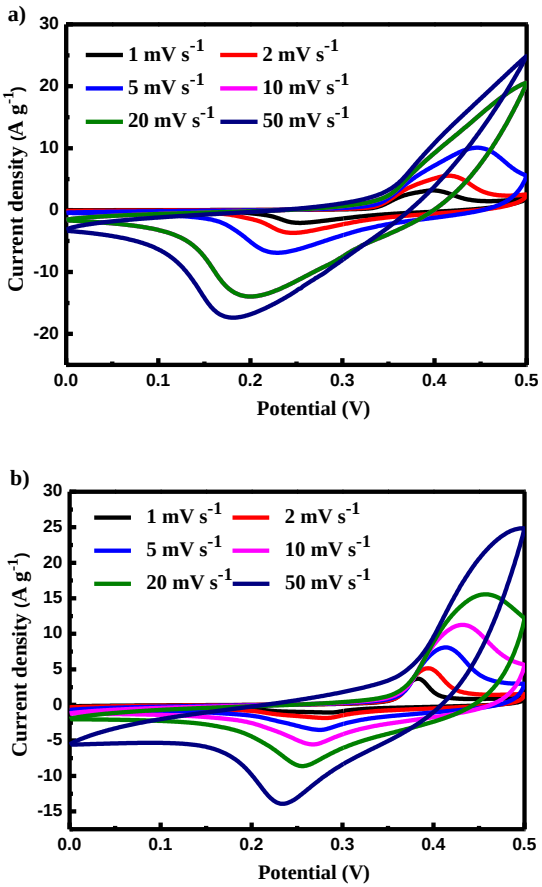


**Figure S8.** Cyclic voltammetry curves of the **1a** in a three-electrode system at different scan rates a) before and b) after 13,000 cycling of charge and discharge at 5 A $g^{-1}$.

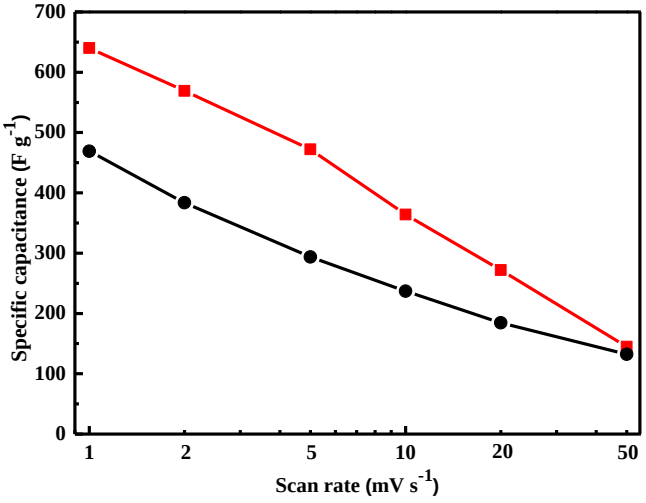


**Figure S9.** Rate-dependent specific capacitance upon increase of scan rate of **1a** before (red) and after (black) 13,000 cycling of charge and discharge at 5 A $g^{-1}$.

**Table S6.** Specific capacitance of **1a** with different scan rates.

| Scan rates (mV $s^{-1}$) | C (Before) (F $g^{-1}$) | C (After) (F $g^{-1}$) |
|---|---|---|
| 1 | 640.0 | 469.0 |
| 2 | 569.1 | 383.5 |
| 5 | 472.0 | 293.8 |
| 10 | 364.0 | 237.1 |
| 20 | 272.0 | 184.4 |
| 50 | 145.0 | 132.4 |

For the **1a** sample, the shape of the CV curve remained basically unchanged before and after 13,000 cycles, and there was clear redox peak, indicating the presence of pseudocapacitive properties (Figure S8). Notably, the area of the CV curve decreased after 13,000 cycles, along with a decrease in the peak current. Figure S9 shows the specific capacitance of the samples as a function of scan rate, from which it can be seen that the specific capacitance decreases with increasing scan rate. This is mainly because at higher scan rates, the electrolyte ions do not have enough time to enter the internal active sites of the electrode, resulting in insufficient redox reactions. The specific capacitance calculated according to the CV curve is shown in Table S6, and after 13,000 cycles, the capacitance retention is 73.3% at 1 mV $s^{-1}$, indicating that the sample **1a** has good cycling stability.

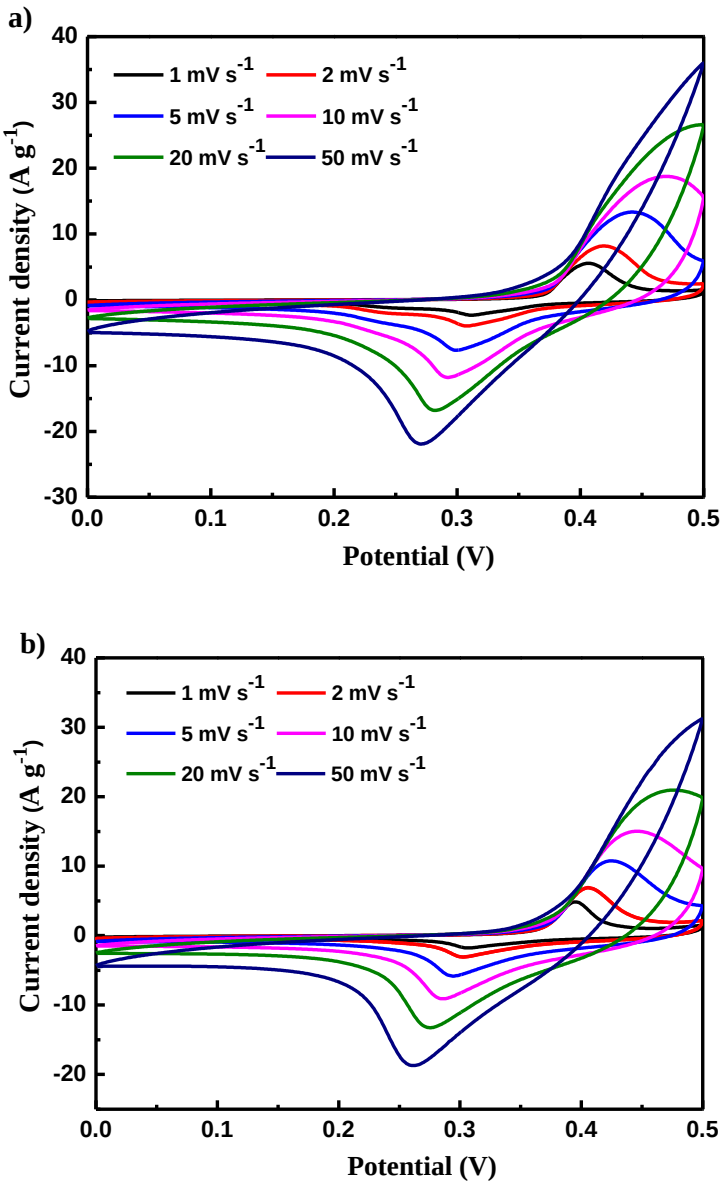


**Figure S10.** Cyclic voltammetry curves of the **1c** in a three-electrode system at different scan rates a) before and b) after 13,000 cycling of charge and discharge at 5 A $g^{-1}$.

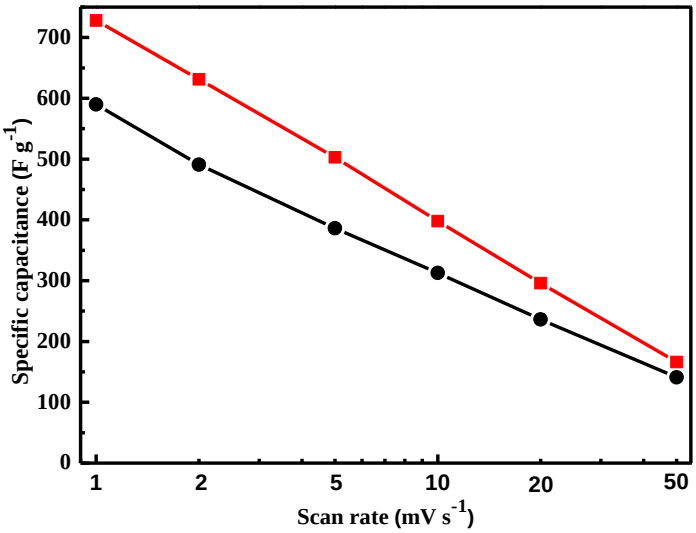


**Figure S11.** Rate-dependent specific capacitance based on scan rate of **1c** before (red) and after (black) 13,000 cycling of charge and discharge at 5 A $g^{-1}$.

**Table S7.** Specific capacitance of **1c** with different scan rates.

| Scan rate (mV $s^{-1}$) | C (Before) (F $g^{-1}$) | C (After) (F $g^{-1}$) |
|---|---|---|
| 1 | 728.0 | 590.0 |
| 2 | 631.0 | 491.0 |
| 5 | 502.8 | 386.2 |
| 10 | 398.0 | 312.9 |
| 20 | 295.9 | 236.4 |
| 50 | 166.2 | 140.8 |

As shown in Figure S10, the shape of the CV curves of the **1c** sample before and after 13,000 cycles remained basically unchanged, and there were obvious redox peaks, indicating the existence of pseudocapacitive properties. Notably, the area of the CV curve decreased after 13,000 cycles, along with a decrease in the peak current. Figure S11 shows the specific capacitance of the samples as a function of scan rate, from which it can be seen that the specific capacitance decreases with increasing scan rate. This is mainly because at higher scan rates, the electrolyte ions do not have

enough time to enter the internal active sites of the electrode, resulting in insufficient redox reactions. By comparing the specific capacitance calculated from the CV curves before and after 13,000 cycling (Table S7), the capacitance retention is 81.0% at 1 mV $s^{-1}$, indicating that the sample **1c** has good cycling stability.

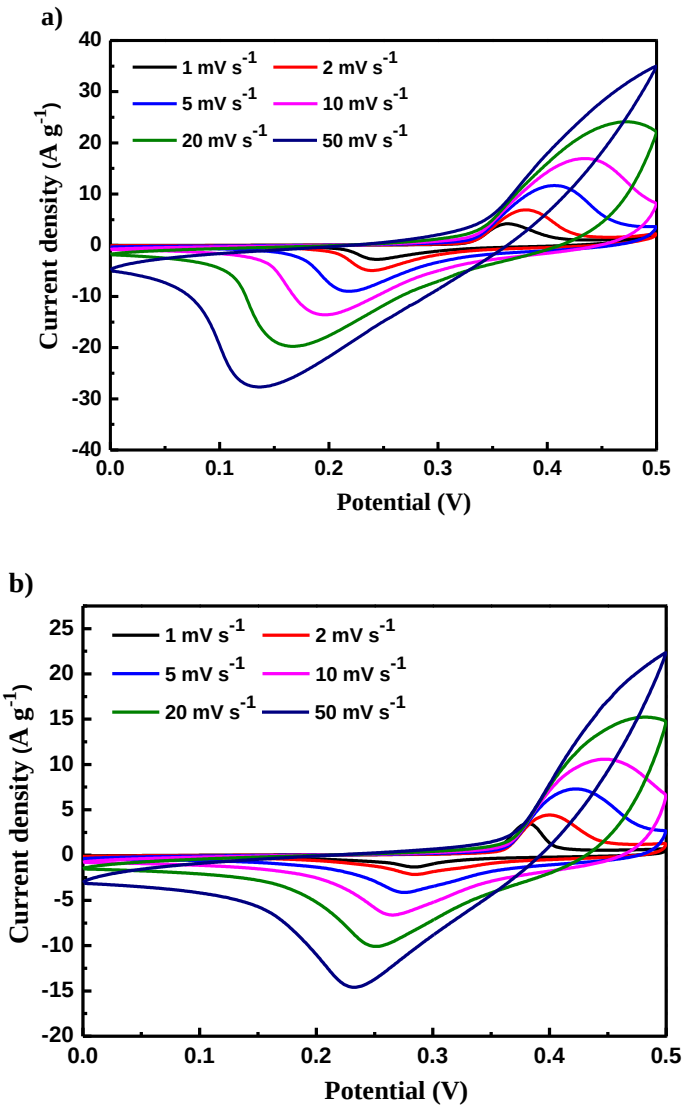


**Figure S12.** Cyclic voltammetry curves of the **2a** in a three-electrode system at different scan rates a) before and b) after 13,000 cycling of charge and discharge at 5 A $g^{-1}$.

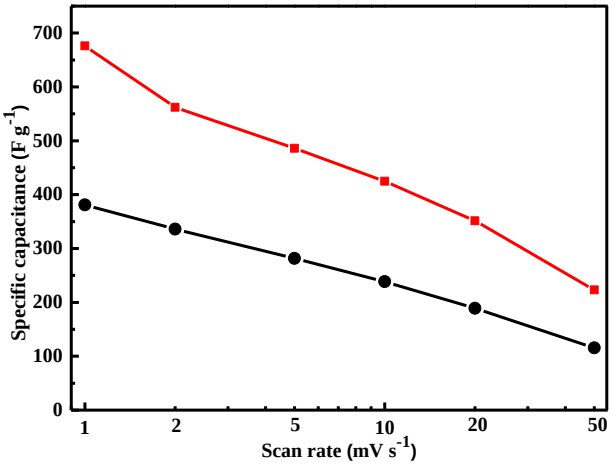


**Figure S13.** Rate-dependent specific capacitance based on scan rate of **2a** electrode before (red) and after (black) 13,000 cycling of charge and discharge at 5 A $g^{-1}$.

**Table S8.** Specific capacitance of **2a** electrode with different scan rates.

| Scan rate (mV $s^{-1}$) | C (Before) (F $g^{-1}$) | C (After) (F $g^{-1}$) |
|---|---|---|
| 1 | 676.0 | 381.0 |
| 2 | 562.0 | 336.0 |
| 5 | 486.0 | 281.8 |
| 10 | 425.0 | 238.5 |
| 20 | 351.5 | 189.0 |
| 50 | 223.2 | 115.6 |

Figure S12 shows the CV curves of the **2a** sample before and after 13,000 cycles. It can be clearly seen that the CV curves had obvious redox peaks, indicating the existence of pseudocapacitive properties, and the shape is basically unchanged before and after cycling. Notably, the area of the CV curve decreased after 13,000 cycles, along with a decrease in the peak current. Figure S13 shows that at higher scan rates, the electrolyte ions do not have enough time to enter the internal active sites of the electrode, resulting in insufficient redox reactions leading to a decrease in capacitance. By comparing the specific capacitance calculated from the CV curves

before and after 13,000 cycling (Table S8), the capacitance retention is 56.4% at 1 mV $s^{-1}$, indicating that the sample **2a** has good cycling stability.

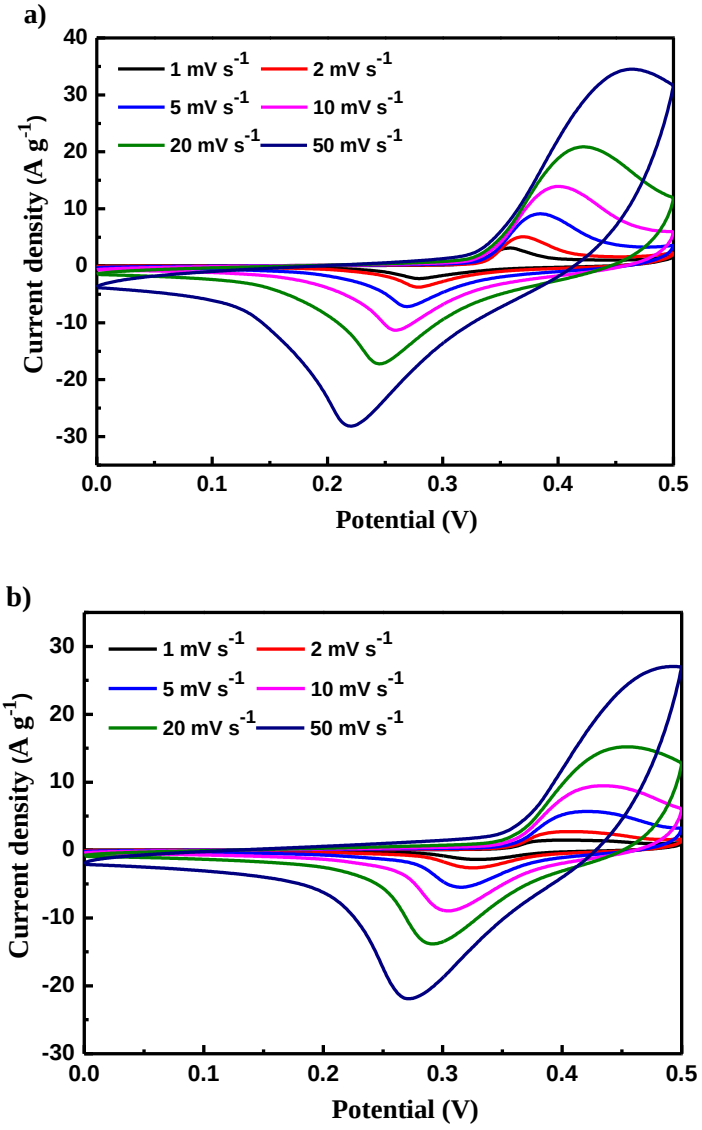


**Figure S14.** Cyclic voltammetry curves of the **2c** electrode in a three-electrode system at different scan rates a) before and b) after 13,000 cycling of charge and discharge at 5 A $g^{-1}$.

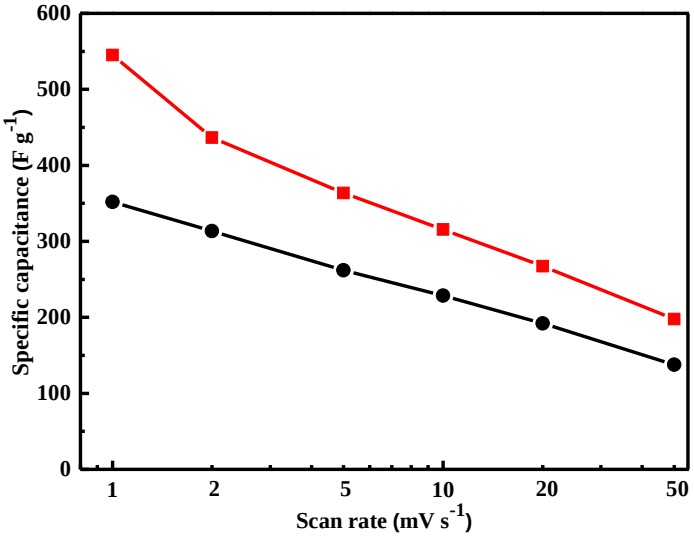


**Figure S15.** Rate-dependent specific capacitance based on scan rate of **2c** electrode before (red) and after (black) 13,000 cycling of charge and discharge at 5 A $g^{-1}$.

**Table S9.** Specific capacitance of **2c** electrode with different scan rates.

| Scan rate (mV $s^{-1}$) | C (Before) (F $g^{-1}$) | C (After) (F $g^{-1}$) |
|---|---|---|
| 1 | 545.0 | 352.0 |
| 2 | 436.5 | 313.5 |
| 5 | 363.5 | 261.8 |
| 10 | 315.6 | 228.6 |
| 20 | 267.2 | 191.9 |
| 50 | 197.6 | 137.8 |

The CV curves of the **2c** sample before and after 13,000 cycles are shown in Figure S14. The CV curves before and after 13,000 cycles can clearly see obvious redox peaks, indicating the existence of pseudocapacitive properties, and the shape is basically unchanged before and after cycling. Figure S15 shows that at higher scan rates, the electrolyte ions do not have enough time to enter the internal active sites of the electrode, resulting in insufficient redox reactions leading to a decrease in capacitance. The specific capacitance calculated according to the CV curve is

shown in Table S9, and after 13,000 cycles, the capacitance retention is 64.6% at 1 mV $s^{-1}$, indicating that the sample has good cycling stability.

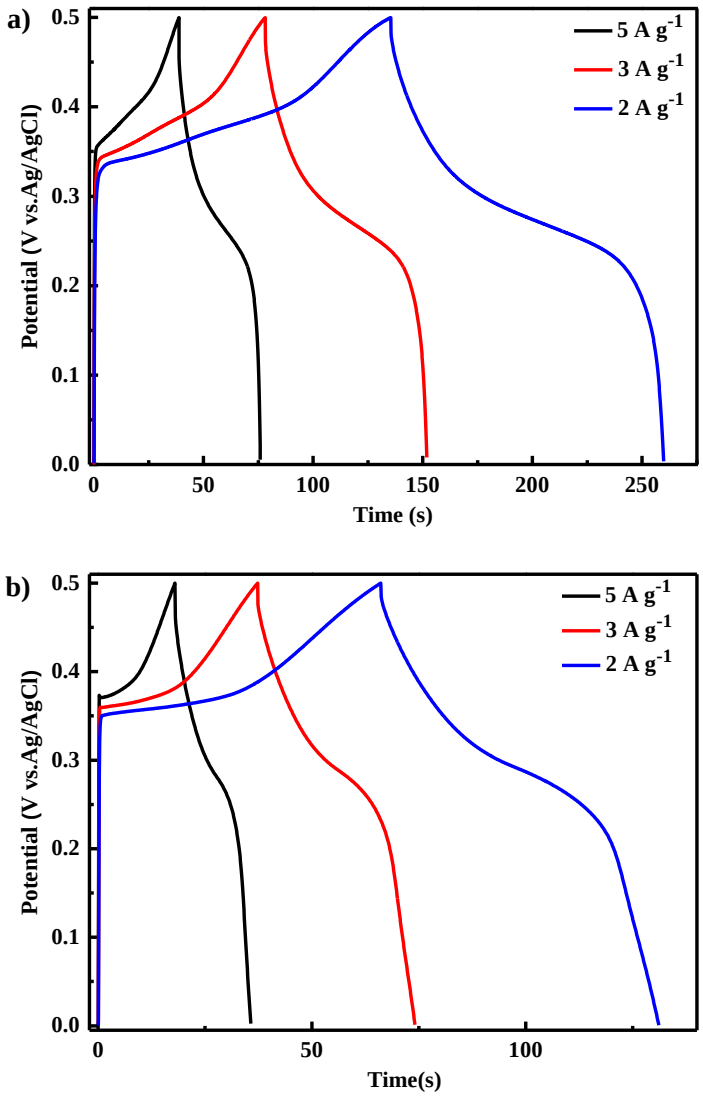


**Figure S16.** Galvanostatic charge and discharge curves at current densities of 2, 3 and 5 A $g^{-1}$ a) before and b) after 13,000 cycling of charge and discharge at 5 A $g^{-1}$ for **1a** electrode.

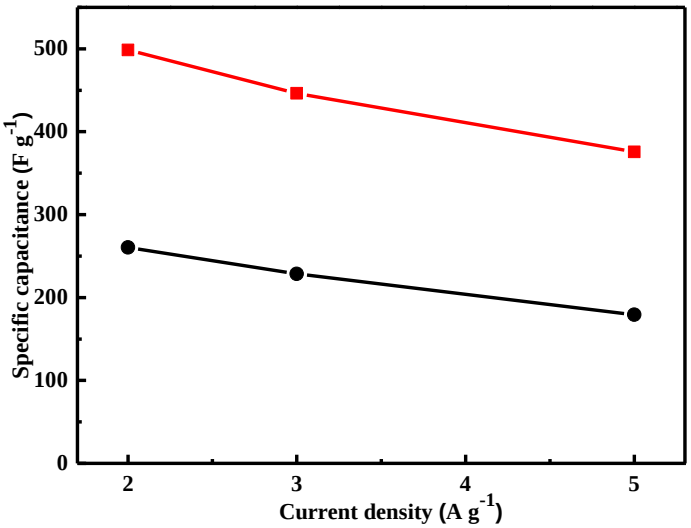


**Figure S17.** Rate-dependent specific capacitance upon increase of current density of **1a** electrode before (red) and after (black) 13,000 cycling of charge and discharge at 5 A $g^{-1}$.

**Table S10.** Specific capacitance of **1a** with different current density.

| **Current density (A $g^{-1}$)** | **C (Before) (F $g^{-1}$)** | **C (After) (F $g^{-1}$)** |
|---|---|---|
| 2 | 499.0 | 260.3 |
| 3 | 446.3 | 228.4 |
| 5 | 375.6 | 179.2 |
| Rate capability (2-5 A $g^{-1}$) | 75.3% | 68.8% |

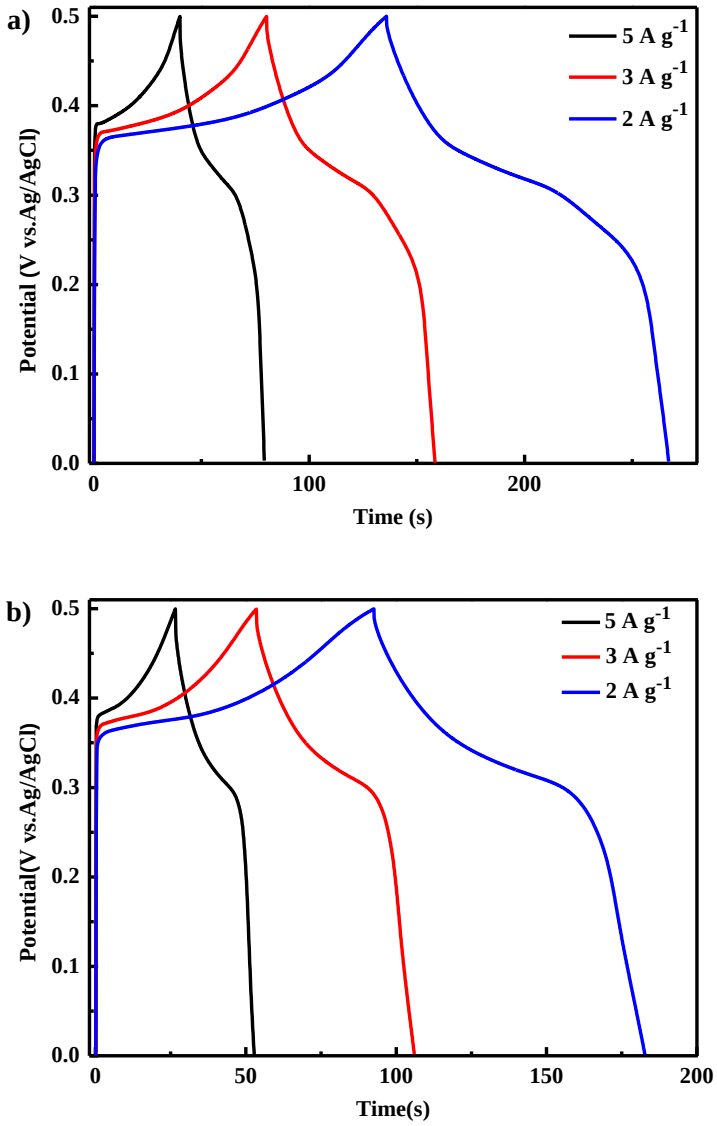


**Figure S18.** Galvanostatic charge and discharge curves at current densities of 2, 3, and 5 for **1c** electrode a) before and b) after 13,000 cycling of charge and discharge at 5 A $g^{-1}$.

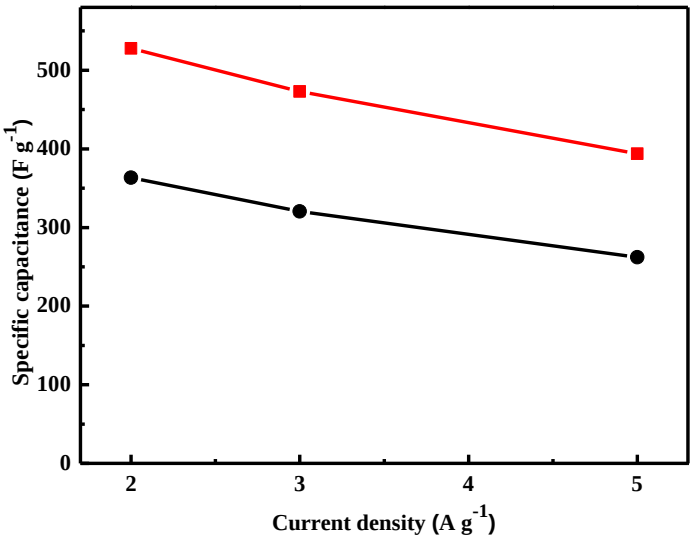


**Figure S19.** Rate-dependent specific capacitance upon increase of current density of **1c** electrode before (red) and after (black) 13,000 cycling of charge and discharge at 5 A $g^{-1}$.

**Table S11.** Specific capacitance of **1c** electrode with different current density.

| **Current density (A $g^{-1}$)** | **C (Before) (F $g^{-1}$)** | **C (After) (F $g^{-1}$)** |
|---|---|---|
| 2 | 528.0 | 363.0 |
| 3 | 473.1 | 320.5 |
| 5 | 393.8 | 262.3 |
| Rate capability (2-5 A $g^{-1}$) | 74.6% | 72.3% |

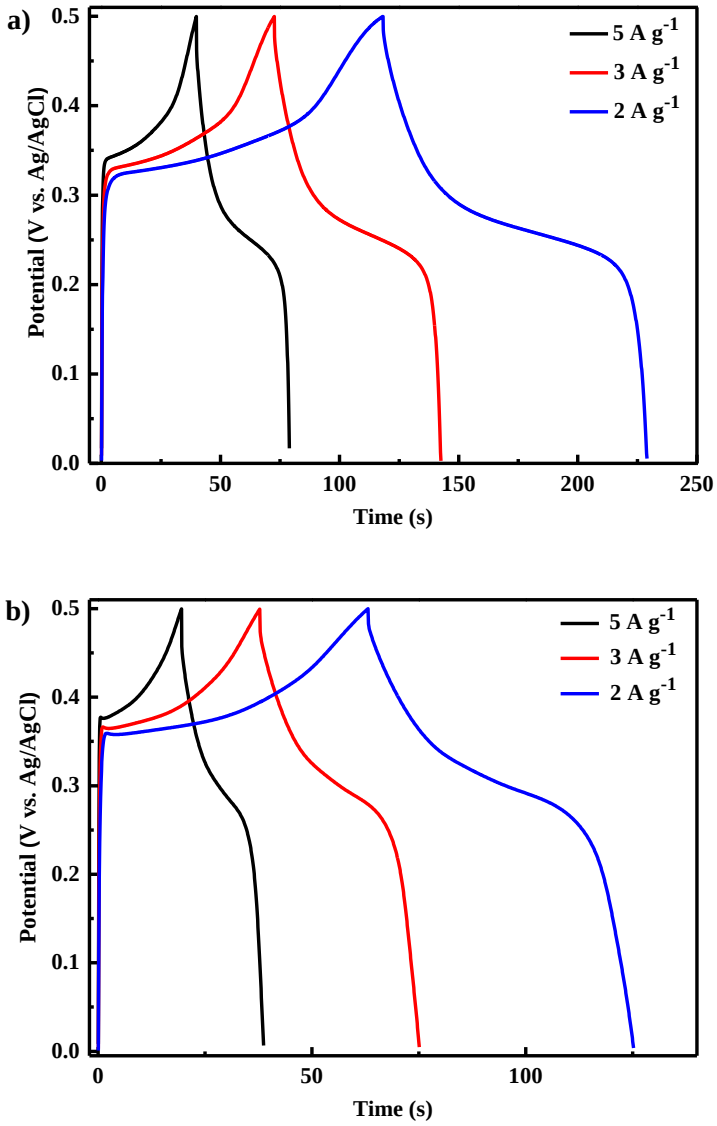


**Figure S20.** Galvanostatic charge and discharge curves at current densities of 2, 3 and 5 A $g^{-1}$ for **2a** electrode a) before and b) after 13,000 cycling of charge and discharge at 5 A $g^{-1}$.

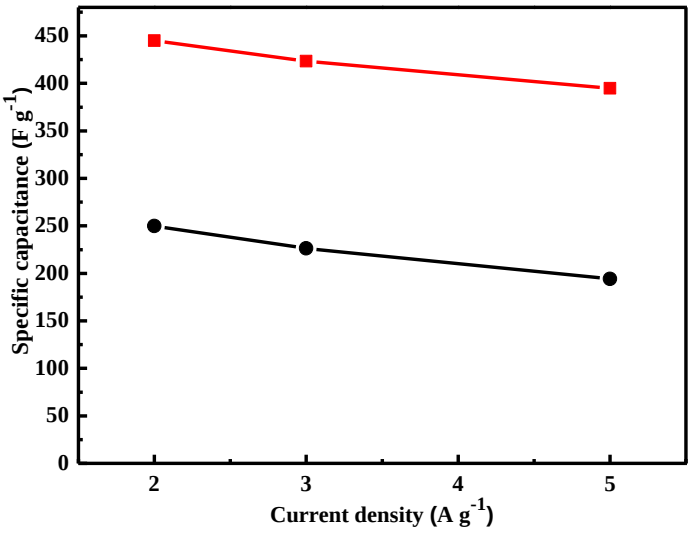


**Figure S21.** Rate-dependent specific capacitance upon increase of current density of **2a** electrode before (red) and after (black) 13,000 cycling of charge and discharge at 5 A $g^{-1}$.

**Table S12.** Specific capacitance of **2a** electrodes with different current density.

| **Current density (A $g^{-1}$)** | **C (Before) (F $g^{-1}$)** | **C (After) (F $g^{-1}$)** |
|---|---|---|
| 2 | 445.0 | 249.8 |
| 3 | 423.3 | 226.4 |
| 5 | 394.9 | 194.1 |
| Rate capability (2-5 A $g^{-1}$) | 88.8% | 77.7% |

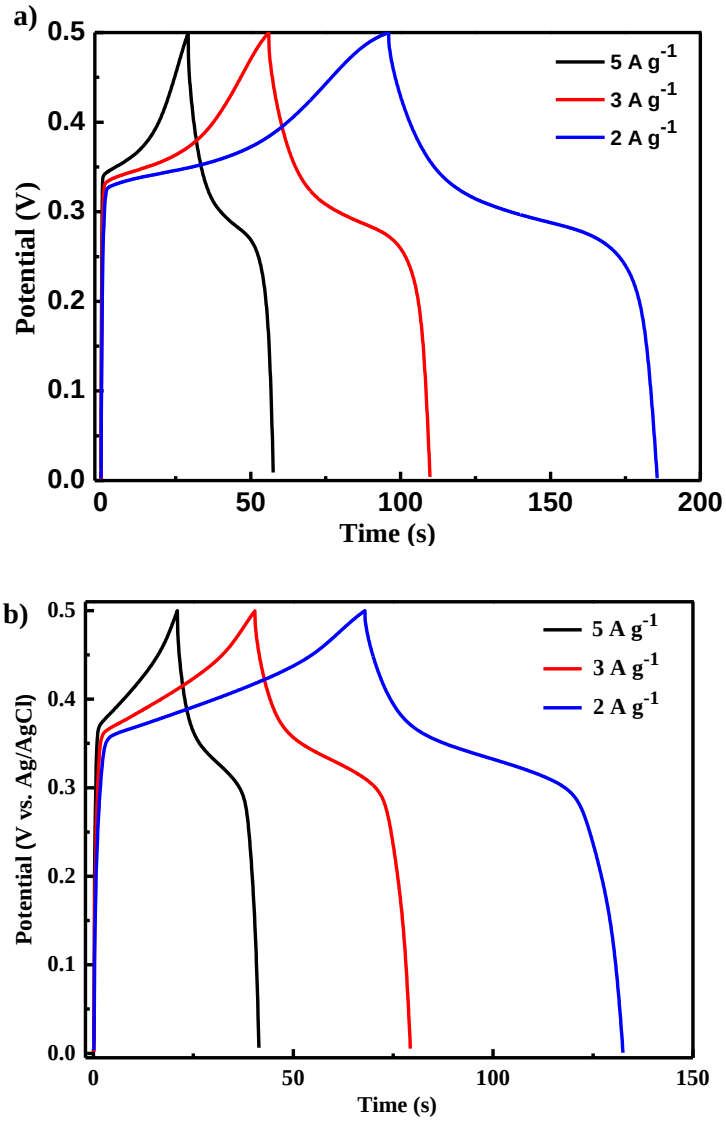


**Figure S22.** Galvanostatic charge and discharge curves at current densities of 2, 3 and 5 A $g^{-1}$ for **2c** electrode a) before and b) after 13, 000 cycling of charge and discharge at 5 A $g^{-1}$.

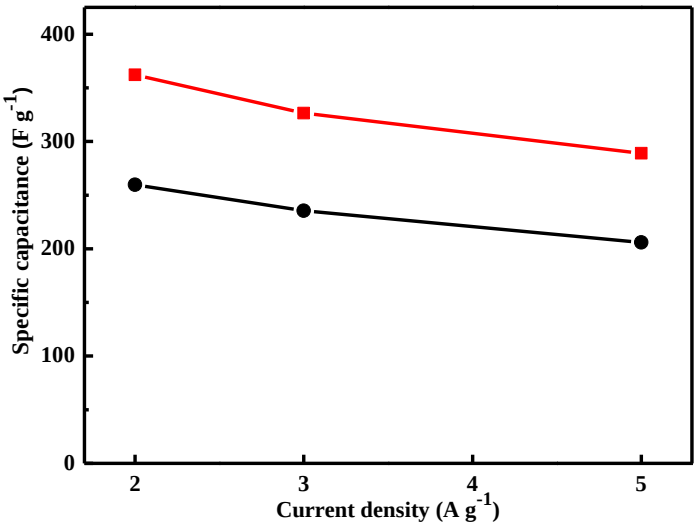


**Figure S23.** Rate-dependent specific capacitance upon increase of current density of **2c** electrode before (red) and after (black) 13,000 cycling of charge and discharge at 5 A $g^{-1}$.

**Table S13.** Specific capacitance of **2c** electrode with different current density.

| **Current density (A $g^{-1}$)** | **C (Before) (F $g^{-1}$)** | **C (After) (F $g^{-1}$)** |
|---|---|---|
| 2 | 362.0 | 259.6 |
| 3 | 326.4 | 235.5 |
| 5 | 289.0 | 206.0 |
| Rate capability (2-5 A $g^{-1}$) | 79.8% | 79.4% |

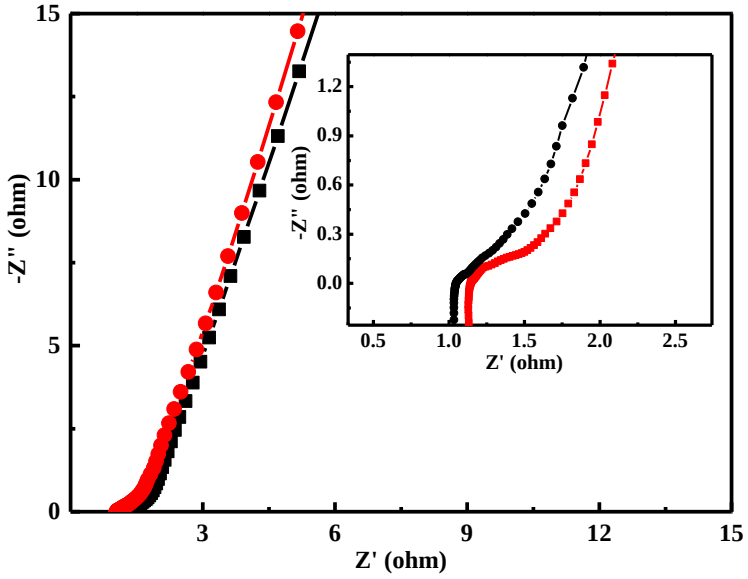


**Figure S24.** Nyquist electrochemical impedance spectra of the **1a** electrode in a three-electrode system before (red) and after (black) 13,000 cycling of charge and discharge at 5 A $g^{-1}$.

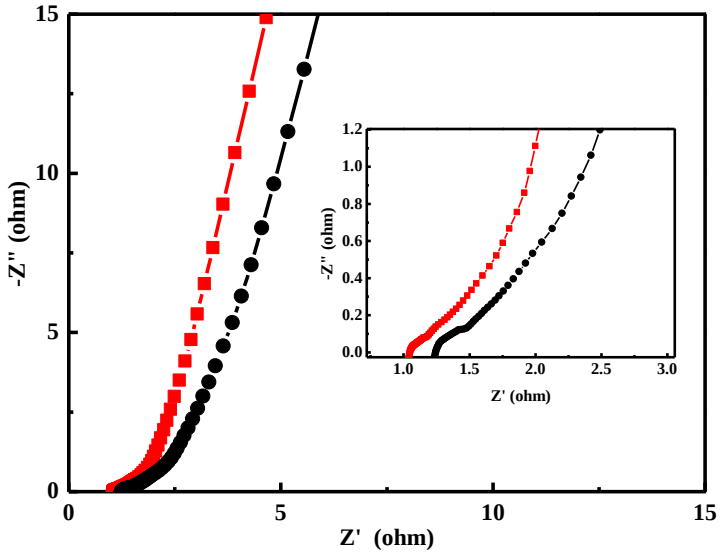


**Figure S25.** Nyquist electrochemical impedance spectra of the **1c** electrode in a three-electrode system before (red) and after (black) 13,000 cycling of charge and discharge at 5 A $g^{-1}$.

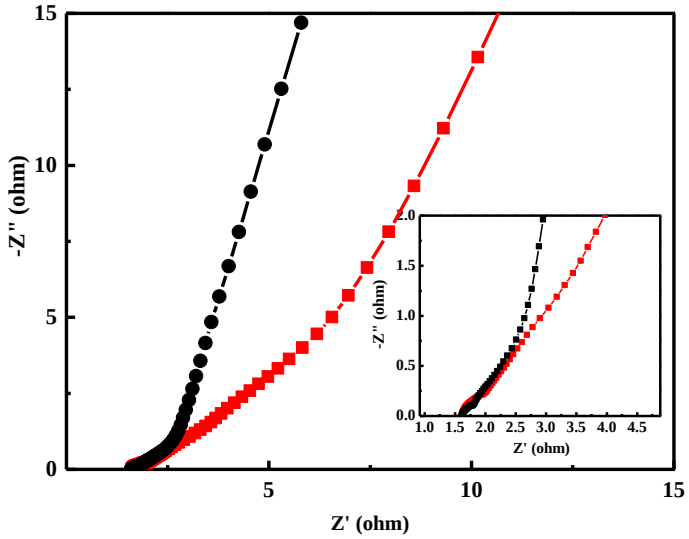


**Figure S26.** Nyquist electrochemical impedance spectra of the **2a** electrode in a three-electrode system before (red) and after (black) 10,000 cycling of charge and discharge at 5 A $g^{-1}$.

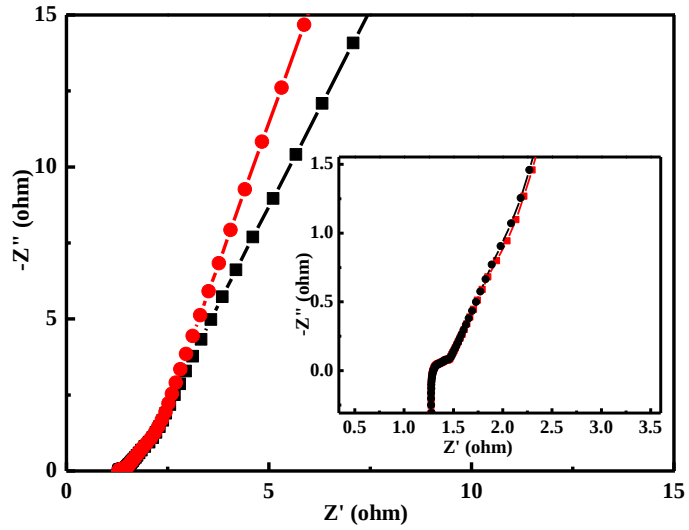


**Figure S27.** Nyquist electrochemical impedance spectra of the **2c** electrode in a three-electrode system before (red) and after (black) 13,000 cycling of charge and discharge at 5 A $g^{-1}$.

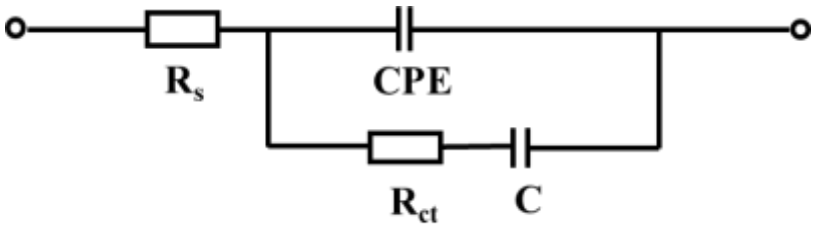


**Figure S28.** Equivalent circuit diagram

**Table S14.** Estimated $R_s$ and $R_{ct}$ values for **1a**, **1c**, **2a** and **2c**.

| **Samples** | **Before cycle** | | **After cycle** | |
|---|---|---|---|---|
| | **$R_s$ (Ω)** | **$R_{ct}$ (Ω)** | **$R_s$ (Ω)** | **$R_{ct}$ (Ω)** |
| **1a** | 1.2 | 1.3 | 1.1 | 2.2 |
| **1c** | 1.0 | 2.2 | 1.1 | 2.5 |
| **2a** | 1.7 | 2.7 | 1.7 | 2.4 |
| **2c** | 1.2 | 2.3 | 1.4 | 2.1 |

# References

1 K. B. Thapa, B. Chen, L. Bian, Y. Xu, J. He, W. Huang, Q. Ju and Z. Fang, *ACS Appl. Mater. Interfaces*, 2021, **13**, 35905-35913.
2 M. Zhang, K. Chen, C. Wang, M. Jian, Z. Yin, Z. Liu, G. Hong, Z. Liu and Y. Zhang, *Small*, 2018, **14**, 1801009.